

Internal tide generation by abyssal hills using analytical theory

Angélique Melet,¹ Maxim Nikurashin,^{2,3} Caroline Muller,⁴ S. Falahat,⁵ Jonas Nycander,⁵ Patrick G. Timko,⁶ Brian K. Arbic,⁷ and John A. Goff⁸

Received 14 June 2013; revised 28 October 2013; accepted 28 October 2013; published 26 November 2013.

[1] Internal tide driven mixing plays a key role in sustaining the deep ocean stratification and meridional overturning circulation. Internal tides can be generated by topographic horizontal scales ranging from hundreds of meters to tens of kilometers. State of the art topographic products barely resolve scales smaller than ~ 10 km in the deep ocean. On these scales abyssal hills dominate ocean floor roughness. The impact of abyssal hill roughness on internal-tide generation is evaluated in this study. The conversion of M_2 barotropic to baroclinic tidal energy is calculated based on linear wave theory both in real and spectral space using the Shuttle Radar Topography Mission SRTM30_PLUS bathymetric product at $1/120^\circ$ resolution with and without the addition of synthetic abyssal hill roughness. Internal tide generation by abyssal hills integrates to 0.1 TW globally or 0.03 TW when the energy flux is empirically corrected for supercritical slope (i.e., $\sim 10\%$ of the energy flux due to larger topographic scales resolved in standard products in both cases). The abyssal hill driven energy conversion is dominated by mid-ocean ridges, where abyssal hill roughness is large. Focusing on two regions located over the Mid-Atlantic Ridge and the East Pacific Rise, it is shown that regionally linear theory predicts an increase of the energy flux due to abyssal hills of up to 100% or 60% when an empirical correction for supercritical slopes is attempted. Therefore, abyssal hills, unresolved in state of the art topographic products, can have a strong impact on internal tide generation, especially over mid-ocean ridges.

Citation: Melet, A., M. Nikurashin, C. Muller, S. Falahat, J. Nycander, P. G. Timko, B. K. Arbic, and J. A. Goff (2013), Internal tide generation by abyssal hills using analytical theory, *J. Geophys. Res. Oceans*, 118, 6303–6318, doi:10.1002/2013JC009212.

1. Introduction

[2] Turbulent mixing across density surfaces is thought to be the primary driver of the abyssal limb of the meridional overturning circulation and associated deep stratification [Munk and Wunsch, 1998; Nikurashin and Ferrari, 2013; Talley, 2013]. The additional contribution to the upper limb of the overturning circulation and the mid-depth

stratification comes from the wind-induced upwelling in the Southern Ocean [Toggweiler and Samuels, 1995; Gnanesikan, 1999; Marshall and Speer, 2012]. In the ocean interior, diapycnal mixing is mainly sustained by breaking internal waves [Garrett and Kunze, 2007]. Among the different classes of internal waves, internal tides are especially important: it has been estimated that their breaking provides around 1 terawatts (TW, $1 \text{ TW} = 10^{12} \text{ W}$) out of the 3 ± 1 TW of energy dissipation needed in the ocean interior to maintain the deep ocean stratification [e.g., Munk and Wunsch, 1998; Egbert and Ray, 2001; Jayne and St. Laurent, 2001; St. Laurent and Simmons, 2006]. Internal-tide driven mixing, parameterized in most recent AR5 IPCC-class climate models with a semiempirical parameterization [St. Laurent et al., 2002], has been shown to impact the large-scale ocean circulation and improve climate simulations [e.g., Simmons et al., 2004a; Saenko and Merryfield, 2005; Jayne, 2009]. Therefore, understanding energy conversion from the barotropic tides into internal tides and the corresponding distribution of turbulent mixing in the ocean remains a key issue for accurate simulations of ocean circulation and climate.

[3] Internal tides are internal waves generated by the interaction of barotropic tides with rough topography having horizontal scales from a few hundreds of meters to a few tens of kilometers [e.g., Bell, 1975a]. The internal tide generation problem has been addressed in several theoretical, inverse and modeling studies. From astronomical

¹Program in Atmospheric and Oceanic Sciences, Princeton University, Princeton, New Jersey, USA.

²Institute for Marine and Antarctic Studies, University of Tasmania, Hobart, Tasmania, Australia.

³ARC Centre of Excellence for Climate System Science, Australia.

⁴CNRS/Laboratoire d'Hydrodynamique de l'Ecole Polytechnique, Palaiseau, France.

⁵Department of Meteorology, Stockholm University, Stockholm, Sweden.

⁶Centre for Applied Marine Sciences, Bangor University, Menai Bridge, UK.

⁷Department of Earth and Environmental Sciences, University of Michigan, Ann Arbor, Michigan, USA.

⁸Institute for Geophysics, Jackson School of Geosciences, The University of Texas at Austin, Austin, Texas, USA.

Corresponding author: A. Melet, NOAA/Geophysical Fluid Dynamics Laboratory, Princeton University Forrestal Campus, 201 Forrestal Road, Princeton, NJ 08540, USA. (amelet@princeton.edu)

observations, it is known that energy dissipation of the M_2 tidal constituent accounts for 2.4 TW, about 2/3 of the dissipation over all constituents [Munk, 1997]. This dissipation is due to both bottom friction, a process especially important in shallow seas, and internal tide generation over rough topography. Through inverse calculations using altimeter data, Egbert and Ray [2000, 2001] inferred that about 25–30% of the tidal energy dissipation occurs in the deep ocean, where internal tide generation is thought to be the dominant process for energy dissipation. High levels of mixing were observed in the Brazil Basin several thousands of meters above rough topography [Polzin et al., 1997] and were indeed likely due to the breaking of locally generated internal tides. However, the spatial resolution of such inverse estimates is low. Hence, they do not resolve the fine-scale distribution of the energy conversion, which appears to be patchy, reflecting the patchiness of topographic roughness. Spatial resolution is also a limiting factor for the study of the energy conversion from barotropic to internal tides using numerical global baroclinic tide models. Another limitation of early numerical global baroclinic tide models [e.g., Arbic et al., 2004; Simmons et al., 2004b] is their employment of a horizontally uniform stratification due to the lack of atmospheric forcing necessary to sustain a realistic horizontally varying stratification.

[4] The energy conversion into internal tides can also be calculated analytically. A linear wave theory was developed by Bell [1975a, 1975b], with refinements provided for instance by Llewellyn Smith and Young [2002] and Khattiwala [2003] to relax assumptions of an infinite depth ocean and uniform stratification. While in an infinite-depth ocean internal tides can radiate from all scales of topography (e.g., Bell [1975a, 1975b]), it was found that the main effect of the finite depth of the ocean is that the conversion by topographic wavelengths longer than the horizontal wavelength of the first internal wave mode (i.e., tens of kilometers) is suppressed [Llewellyn Smith and Young, 2002].

[5] The best topographic products currently available over the global ocean are given on a grid at $1/120^\circ$ (<1 km) (e.g., GEBCO_08 [IOC, IHO and BODC, 2003], SRTM30_PLUS [Becker et al., 2009; Sandwell and Smith, 2009]). Two different types of data are merged within these products: estimates of the bathymetry derived from satellite gravity data, and acoustic soundings performed from ships. The resolution of satellite derived bathymetry is limited to scales larger than 10 km in the deep ocean [Smith and Sandwell, 1997], whereas singlebeam and multibeam acoustic soundings can resolve topographic scales of $O(100)$ m. While more accurate, multibeam acoustic soundings only cover a small fraction of the global ocean ($\sim 10\%$, Charette and Smith [2010]), with most observed regions lying in coastal zones. Therefore, in most of the deep ocean (where acoustic soundings are not available), the effective feature resolution of the best currently available bathymetric product is closer to 10 km than to $1/120^\circ$ (~ 1 km). At scales smaller than 10 km, abyssal hills are the dominant roughness fabric over much of the ocean floor [e.g., Macdonald et al., 1996]. Formed at mid-ocean ridge spreading centers by volcanism and tectonics, they are rafted away by plate spreading and modified through time by mass wasting and sedimentation. Abyssal hills typically

have heights of order 50 m and horizontal scales of order 1–10 km. Therefore, abyssal hill roughness is very poorly represented in standard bathymetric products.

[6] The importance of small-scale topographic roughness for internal tide generation has been suggested in earlier studies. Using linear theory, Nycander [2005] highlighted significant contribution to the energy flux from barotropic to internal tides over the global ocean from scales near the resolution limit of bathymetric data sets (i.e., near scales of 10 km). This implies that a larger flux is likely to be obtained from a topographic data set that includes abyssal hills. Carter et al. [2008] showed that increasing the resolution of their internal tide model from 4 to 1 km results in 20% larger barotropic-to-baroclinic tidal energy conversion. In a recent process oriented study, Iwamae and Hibiya [2012] showed that the energy conversion from the barotropic to baroclinic tide is enhanced by 70% in the Brazil Basin when small-scale topography (between 250 and 2 km) is taken into account. Recent theoretical [Muller and Bühler, 2009; Polzin, 2009] and numerical [Nikurashin and Legg, 2011] studies also suggest that the local breaking of internal waves and hence mixing are sustained primarily by internal tides radiated from abyssal hills.

[7] The present study aims at evaluating the impact of small-scale topographic roughness due to abyssal hills on internal tide generation using direct calculations based on linear wave theory. Although direct observations of abyssal hills are not available on a global scale, it is possible to predict the statistical parameters of abyssal hill roughness world-wide via relationships between the average statistical properties of abyssal hills and the seafloor spreading rate and direction [Goff and Arbic, 2010, hereafter GA]. GA modified these roughness parameters to account for sediment thickness. Using the Shuttle Radar Topography Mission SRTM30_PLUS bathymetric product with and without the addition of synthetic abyssal hill roughness (as described in section 2), we use direct calculations based on linear theory to evaluate the impact of abyssal hills on internal-tide generation for the M_2 tidal component. In section 3, calculations are first performed in real space over two regions having different topographic roughness, located over the Mid-Atlantic Ridge (MAR) and East Pacific Rise (EPR). These calculations allow us to test our methodology and provide some insight on the contribution to the energy flux from different topographic scales. An assessment of the energy flux due to supercritical slopes, where linear theory is not formally valid, is also provided regionally. A correction is then attempted for the overprediction of the energy flux at supercritical slopes. Global calculations are then performed in both real and spectral spaces to assess the impact of abyssal hill roughness on internal-tide generation over the global ocean (section 4).

2. Methodology

2.1. Linear Theory

[8] In this study, we use a synthetic realization of the abyssal hill distribution in real space inferred from the prediction of their statistical parameters (GA). The synthetic abyssal hills are overlaid on a standard topographic product in real space. However, the calculation of the energy

conversion into internal tides, E_f is traditionally done in spectral space [e.g., *Bell*, 1975b; *St. Laurent and Garrett*, 2002]. Moreover, since synthetic abyssal hill topography represents a single realization of the abyssal hill spectrum, we complement the energy flux calculation into M_2 internal tides in the real space with a similar calculation in spectral space.

2.1.1. Calculation in Real Space

[9] The calculation of the energy flux E_f into internal tides at the fundamental M_2 frequency in real space is based on the formulation provided by *Nycander* [2005]. It is given by the sum of the contributions E_f^+ , due to the tidal velocity along the major axis of the tidal ellipse and E_f^- , due to the tidal velocity along the minor axis of the tidal ellipse:

$$E_f^+(\mathbf{r}) = \frac{\rho_0 N_B U_+^2}{4\pi} \sqrt{1 - \frac{f^2}{\omega^2}} \frac{\partial h(\mathbf{r})}{\partial x} \iint \left(g_a(|\mathbf{r} - \mathbf{r}'|) \frac{\partial h(\mathbf{r}')}{\partial x'} \right) d\mathbf{r}' \quad (1)$$

where ρ_0 is a reference density for seawater, ω is the M_2 tidal frequency, U_+ is the amplitude of the semimajor axis of the barotropic M_2 tidal velocity, and the x axis has been chosen to lie along the major axis of the tidal ellipse. N_B is the buoyancy frequency at the sea floor and f is the Coriolis parameter. h is the bottom topography, and the root mean square of h defines the topographic roughness. g_a is a high-pass filter whose definition and necessity are described in the following paragraph. \mathbf{r} and \mathbf{r}' are vectors in the tidal ellipse coordinates space ($\mathbf{r} = x \mathbf{e}_x + y \mathbf{e}_y$, with \mathbf{e}_x and \mathbf{e}_y being, respectively, the unit vectors along the major and minor axes of the tidal ellipse). The double integral is a spatial integral over the ocean. E_f^+ is in units of W m^{-2} . E_f^- is given by a similar expression with U_+ replaced by U_- and x by y , with U_- the amplitude of the semiminor axis of the barotropic M_2 tidal velocity (which is along the y axis).

[10] The convolution integral in equation (1) expresses the fact that wave generation is a nonlocal process where the energy flux at a point depends on the topography in a region around that point. Since only topographic horizontal scales that are shorter than the horizontal wavelength of the first internal tide mode can radiate internal tides in an ocean of finite depth [*Llewellyn Smith and Young*, 2002], *Nycander* [2005] used a Gaussian high-pass filter, $g_a(\mathbf{r})$, to suppress the radiation from long topographic scales. The cutoff length of the filter, a , is given by:

$$a = \frac{\beta}{\pi \sqrt{\omega^2 - f^2}} \int_{-D}^0 N(z) dz. \quad (2)$$

[11] In equation (2), N is the buoyancy frequency, D is the local depth of the ocean, and β is a nondimensional parameter set to 1.45. The cutoff length a is proportional to the horizontal wavelength of the first internal wave mode, and has typical values of $\text{O}(10)$ km. Note that for the actual calculation, an equivalent of equation (1) involving a partial integration is used (see *Nycander* [2005] for more details) and the equation has been transformed to the longitude-latitude coordinate system. Moreover, the finite difference scheme used in this study has been improved

compared to *Nycander* [2005] according to the work of *Green and Nycander* [2013].

2.1.2. Calculation in Spectral Space

[12] The calculation of the energy flux E_f into internal tides in spectral space is based on *Bell* [1975b]'s theory, with vertical scales longer than the local ocean depth being removed:

$$E_f = \frac{\rho_0}{2\pi^2} \sum_{n=1}^{n=n_N} n\omega [(N_B^2 - n^2\omega^2)(n^2\omega^2 - f^2)]^{1/2} \iint \kappa^{-1} J_n^2 \left(\frac{[U_+^2 k^2 + U_-^2 l^2]^{1/2}}{\omega} \right) \Phi(\mathbf{k}) d\mathbf{k} dl. \quad (3)$$

[13] In equation (3), J_n is the Bessel function of the first kind of order n . $\mathbf{k} = (k, l)$ is the wavenumber of the topography and $\kappa = (k^2 + l^2)^{1/2}$. $\Phi(\mathbf{k})$ is the spectrum of the topography. The integral over the wavenumber of the topography starts from (k_0, l_0) , the smallest topographic wavenumber involved in the generation of internal waves in a finite depth ocean. Note that in this study, the square root of the integral of the topographic spectrum in the abyssal hills wavenumber range defines the abyssal hill roughness in spectral space. The index n corresponds to tidal harmonics, with the maximum harmonic n_N being the largest integer less than N_B/ω (the frequency must fall in the range $f < n\omega < N_B$ for internal tides to propagate). In the following calculations of the energy flux into internal tides based on equation (3), the spectrum of the topography $\Phi(\mathbf{k})$ corresponds to abyssal hills only, and is computed from the *Goff and Jordan* [1988] formulation using the GA parameters of abyssal hill statistics, given on a $1/4^\circ$ grid. Therefore, the spectrum of the bathymetry changes every $1/4^\circ$ and the resolution of the spectrally computed energy flux is $1/4^\circ$.

[14] The calculations of the energy flux into internal tides in real space (1) and spectral space (3) are not strictly equivalent. Differences in the calculations involve the treatment of higher harmonics (small tidal excursion approximation used in equation (1)) and of the ocean finite-depth. Moreover, in the real space calculation the conversion of tidal energy by abyssal hills is estimated by the difference in the energy flux with abyssal hills added to the bathymetric product and the flux without the addition of abyssal hills. In contrast, in the spectral calculation, the conversion due to abyssal hills is estimated from the spectra of the abyssal hill topography only. Despite these minor differences, the estimates of energy conversion by abyssal hills should be reasonably consistent between the two calculations.

2.1.3. Regimes of Linear Theory Validity

[15] Two parameters of dynamical interest for the generation of internal tides are the tidal excursion and the steepness parameters. The tidal excursion parameter, denoted by ζ hereafter, is the ratio of the tidal excursion amplitude, U_0/ω , to the horizontal scale of the bathymetry, L :

$$\zeta = \frac{U_0}{\omega L}, \quad (4)$$

where $U_0 = [U_+^2 + U_-^2]^{1/2}$ is the amplitude of the barotropic tidal velocity.

[16] Internal tides are radiated in both the up- and down-stream directions mainly at the fundamental frequency of the tide, ω , if $\zeta < 1$ (small tidal excursion, acoustic limit), and at its harmonics $n\omega$ if $\zeta > 1$. If the tidal excursion largely exceeds the length scale of the bathymetry ($\zeta \gg 1$), the generated internal waves only propagate in the upstream direction with frequencies $-\kappa U_0$, with κ the amplitude of the wavenumber of the topography. The quasi-steady approximation is valid in this regime and the problem reduces to the generation of steady lee waves. In the open ocean, the tidal excursion rarely exceeds 500 m [Nycander, 2005]. The resolution of our bathymetric product is $1/120^\circ$, i.e., ~ 1 km at the equator, reaching 500 m at 57° in latitude. Therefore, we are in the acoustic regime and the small tidal excursion approximation made in equation (1) is valid in most parts of the ocean. This assumption is further validated in section 4.2.

[17] The steepness parameter, Υ , is the ratio of the topographic slope to the slope of a radiated tidal beam:

$$\Upsilon = \sqrt{\frac{\frac{\partial h^2}{\partial x} + \frac{\partial h^2}{\partial y}}{\frac{\omega^2 - f^2}{N_B^2 - \omega^2}}} \quad (5)$$

[18] This parameter also allows us to distinguish two different regimes. When $\Upsilon > 1$, the topography is referred to as “supercritical”. When $\Upsilon < 1$, the topography is referred to as “subcritical”. For the linear theory to be valid, the topography must be subcritical. Our results are therefore strictly valid only for regions where $\Upsilon < 1$. In section 3, the contribution of regions with supercritical bathymetric slopes to the energy flux into internal tides is evaluated.

2.2. Data sets

2.2.1. Bathymetric Products

[19] In the real space calculation, we use two bathymetric products. The first one is the SRTM30_PLUS bathymetric data set at a resolution of $1/120^\circ$ [Becker et al., 2009; Sandwell and Smith, 2009]. Since bathymetry in the deep ocean is mainly estimated from satellite gravity data, this bathymetric data set does not resolve abyssal hills, except in a few locations where bathymetry was derived from actual acoustic soundings (as indicated by the Survey Identification Data (SID) included in SRTM30_PLUS).

[20] The second bathymetric data set is a blend of the SRTM30_PLUS bathymetry with a synthetic realization of seafloor roughness due to abyssal hills. The synthetic abyssal hill map was produced with the methodology described in GA at a resolution of $1/120^\circ$ to match SRTM30_PLUS. The merging of abyssal hill roughness with SRTM30_PLUS is described in Timko et al. [2009] and Timko et al. (in preparation, 2013). A system of weights based on the SID data is used to prevent the addition of a synthetic roughness field to the SRTM30_PLUS product in locations where high resolution acoustic sounding data, which resolve abyssal hills, were used to derive the depth of the ocean in SRTM30_PLUS. Hereafter, the bathymetric product in which synthetic abyssal hill roughness is overlaid on SRTM30_PLUS is referred to as SSG. An illustration of the bathymetric products is given in Figure 1 for the two regions located over the Mid-Atlantic

Ridge (MAR) and East Pacific Rise (EPR) studied in section 3. The synthetic abyssal hill roughness used in this study is shown in Figure 2. Abyssal hills are morphological indicators of mid-ocean ridge spreading rates and directions. They are linear features, parallel to the ridge at the time of formation, and their heights and widths are inversely correlated to the spreading rate [e.g., Goff, 1991; Small and Sandwell, 1992; Goff et al., 1997]. Therefore, abyssal hills are anisotropic (Figure 1) and have different statistical properties in the parallel and normal to the ridge directions [e.g., Goff and Jordan, 1988; Goff and Arbic, 2010]. In particular, although the overall roughness does not change with direction, characteristic scales will be shortest and slopes steepest in the normal-to-ridge direction, and vice versa in the parallel-to-ridge direction. This anisotropy is taken into account in the GA product and in the energy flux calculations (equations (1) and (3)). The larger abyssal hill topography is associated with regions having lower seafloor spreading rates and less sediment cover, such as the Mid-Atlantic Ridge, the Southwest Indian Ridge and the Central Indian Ridge regions. Abyssal hills are added to deep oceanic regions, largely between 2000 and 6000 m depth (Figure 3). For more details on the abyssal hill roughness realization and distribution, the reader is referred to Goff and Arbic [2010].

2.2.2. Stratification and Tidal Velocities

[21] The bottom and depth-integrated buoyancy frequencies as well as the barotropic M_2 tidal velocities are needed in equations (1–3). The buoyancy frequencies are computed from the World Ocean Circulation Experiment (WOCE) hydrographic atlas [Gouretski and Koltermann, 2004], which is provided on a $1/2^\circ$ grid and 44 vertical levels. The buoyancy frequencies were interpolated onto the $1/120^\circ$ bathymetric grid using the method of Akima [1970]. The barotropic M_2 tidal velocities are provided by the TPXO.6.1 model with a resolution of $1/4^\circ$ [Egbert and Erofeeva, 2002] and are linearly interpolated onto the $1/120^\circ$ bathymetric grid.

3. Results: Regional Estimates

[22] We first focus on two different regions in order to evaluate the impact of different abyssal hill morphologies on internal tide generation and assess the contribution of different spatial scales of bathymetry. An assessment of the energy flux contribution due to supercritical slopes is also provided regionally, and a correction is attempted for the overprediction of the energy flux at supercritical slopes.

[23] The first region studied here is located over the Mid-Atlantic Ridge (MAR), and the second region is located over the East Pacific Rise (EPR). The MAR and EPR represent contrasted cases of mid-ocean ridge topography. The EPR is one of the fastest spreading centers (spreading rate larger than 5 cm/yr), while the MAR is a slow spreading center (spreading rate in the range of 0.5 to 4 cm/yr). Consequently, topographic roughness over the MAR has larger vertical scales and smaller horizontal scales than roughness over the EPR. In the MAR and EPR regions, the crest of the mid-ocean ridge is approximately oriented meridionally (Figure 1). Abyssal hills therefore also tend to be aligned meridionally.

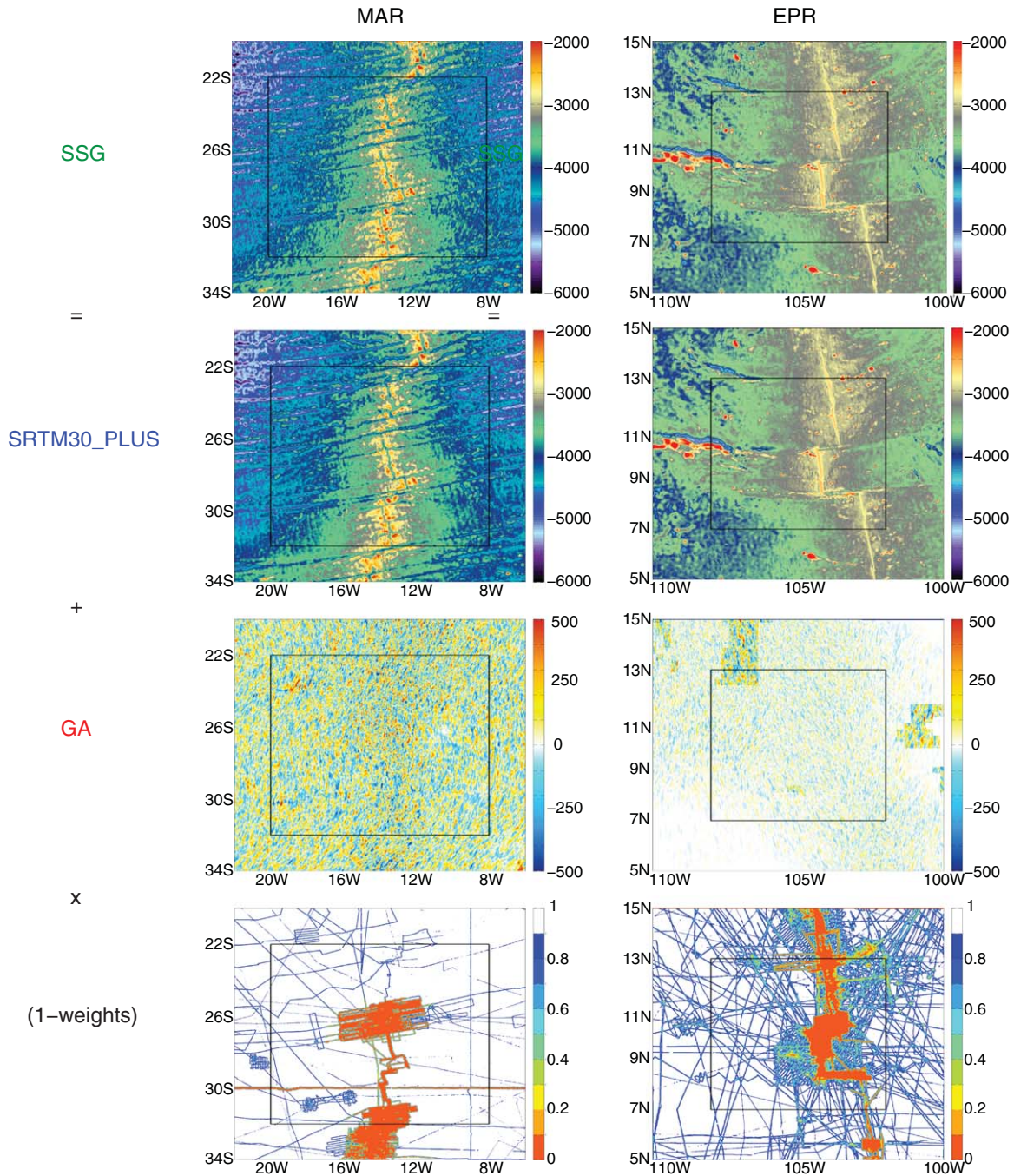


Figure 1. Bathymetric products. Illustration of the merged bathymetry (SSG, top) for which the SRTM30_PLUS product (top middle) is overlaid with synthetic abyssal hill roughness (GA, bottom middle) over the Mid-Atlantic Ridge (MAR, left) and East Pacific Rise (EPR, right) regions used in this study (located by the black boxes). Units are in meters. (bottom) The nondimensional weights, based on the availability of acoustic soundings, used in the merging. Red colors indicate high acoustic data coverage. The regions outside the MAR or EPR boxes represent buffer zones needed for the computation of the convolution in the calculation of the energy flux in real space.

[24] The EPR region studied here extends from 7°N to 13°N, and from 102°W to 108°W. Twenty-five percent of its area (mostly over the ridge) is covered by multibeam data (Figure 1). The MAR region extends from 32°S to 22°S, and from 8°W to 20°W. This region has been the focus of several previous studies related to internal-tide

generation and dissipation [*St. Laurent and Garrett, 2002; Polzin, 2009*] since it is one of the few regions where multibeam data provide high resolution bathymetric data in the deep ocean. Twelve percent of its area (mostly over the ridge) is covered by multibeam data (Figure 1).

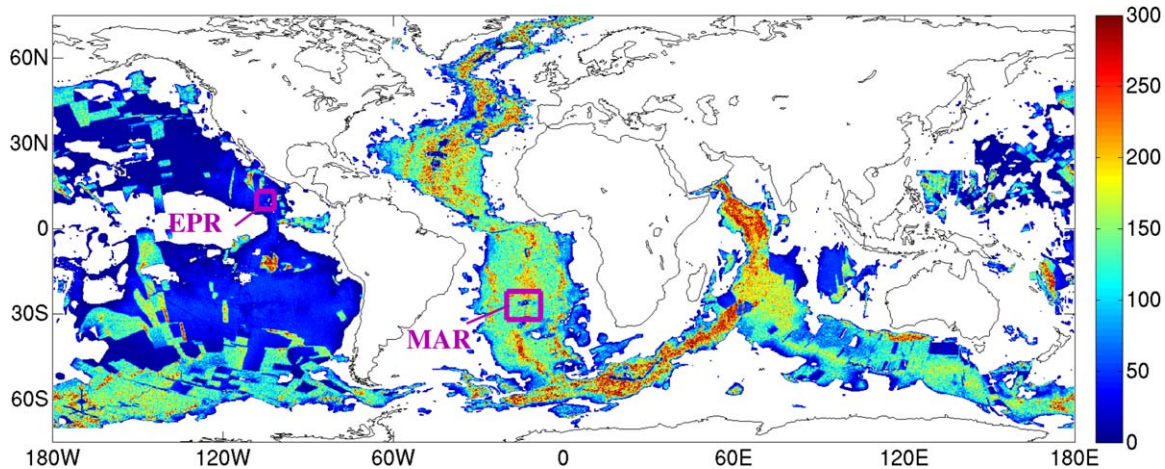


Figure 2. Abyssal hill roughness. Root mean square differences between the SRTM30_PLUS and SSG bathymetric products (in meters) on a $1/4^\circ$ grid (computed with an area weighted mean from the $1/120^\circ$ grid). The purple boxes locate the EPR and MAR regions where regional estimates of energy flux are calculated. Oceanic regions with no values (white regions) are regions where no abyssal hill statistical parameters were available. Areas with small abyssal hill roughness (compared to its surroundings) over midocean ridges are areas where abyssal hills are captured by acoustic data in SRTM30_PLUS.

3.1. Bathymetric Spectra

[25] Bathymetric spectra along the zonal direction for the SRTM30_PLUS, GA, and SSG products over the MAR and EPR regions are shown in Figure 4. In both regions, there is more spectral power density at large horizontal wavelengths ($>10\text{--}30\text{km}$) in the SRTM30_PLUS product than in abyssal hills (Figure 4). At these scales, mid-ocean ridges, fracture zones, and seamounts are the dominant topography. These large features are easily captured by the satellite topography (Figure 1). At smaller horizontal wavelengths ($<10\text{--}30\text{km}$), there is more spectral power density in the synthetic abyssal hills product than in SRTM30_PLUS, reflecting the fact that abyssal hills are the dominant topographic roughness fabric at these scales.

[26] There is not, however, a perfect scale separation between the SRTM30_PLUS and the abyssal hill spectra. The SRTM30_PLUS topography has spectral power density at scales smaller than $O(10)$ km: Outside areas covered by high-resolution acoustic soundings data, the SRTM30_PLUS bathymetry at the limiting scales is a filtered version of the combined effects of small-scale relief (primarily abyssal hills) and altimetric noise. The abyssal hill realization also has spectral power density at scales larger than $O(10)$ km, due to the von Karman spectral model used to represent the abyssal hill statistical behavior in GA. The von Karman model is a band-limited fractal model: it has a power-law form at high wavenumbers, and has a flat “white” spectrum at low wavenumbers (as seen in Figure 4), meaning that all wavenumbers have equal amplitude. The flat spectrum at low wavenumber is necessary because abyssal hill morphology is aperiodic [Goff and Jordan, 1988]. The two spectra therefore overlap, and contribute a small amount of extra power at both high and low wavenumbers. The overlap may be advantageous, however, in the intermediate scales ($O(10\text{--}100)$ km), where spectral power is likely underrepresented by both spectra.

[27] As expected from the different spreading rates of the MAR and EPR, small-scale topographic roughness is larger in the MAR region than in the EPR region, as shown in real space in Figure 1 and by the higher power spectral density in the right plot of Figure 4. Therefore, we expect the M_2 tide energy conversion into internal tides to be more impacted by abyssal hill roughness in MAR than in EPR.

3.2. Energy Conversion

[28] The impact of the addition of synthetic abyssal hill roughness on the energy flux into internal tides is shown in Figure 5 for MAR and EPR. Clearly, abyssal hill roughness strongly influences regional tidal energy conversion. Over the EPR region, the total energy flux into M_2 internal tides is 0.78 GW for the SRTM30_PLUS bathymetry, and 0.95 GW for SSG, which corresponds to an increase of 23% in the tidal energy conversion. As expected (section 3.1), the impact of abyssal hills is much greater in the MAR region, where the total energy flux increases from 4.5 GW with the SRTM30_PLUS bathymetry to 8.5 GW in SSG (an increase of 89%). Note that these values may underestimate the true effect of abyssal hills because portions of the SRTM30_PLUS topography in these regions are derived from acoustic data and hence also resolve abyssal hills.

[29] The conversion of tidal energy over the MAR region with the standard bathymetric product (SRTM30_PLUS) is consistent with the previous estimate by *St. Laurent and Garrett* [2002] of 3.8 ± 1.7 GW, made using the *Smith and Sandwell* [1997] bathymetry. It can also be noted that although the energy flux in the MAR with SRTM30_PLUS is much smoother than with SSG, small-scale energy flux patterns can be spotted even with SRTM30_PLUS in places where multibeam data are included in SRTM30_PLUS (Figure 1, see around $26^\circ\text{S } 14^\circ\text{W}$ and $30\text{--}34^\circ\text{S } 14^\circ\text{W}$ in the MAR region). When abyssal hill roughness is added to

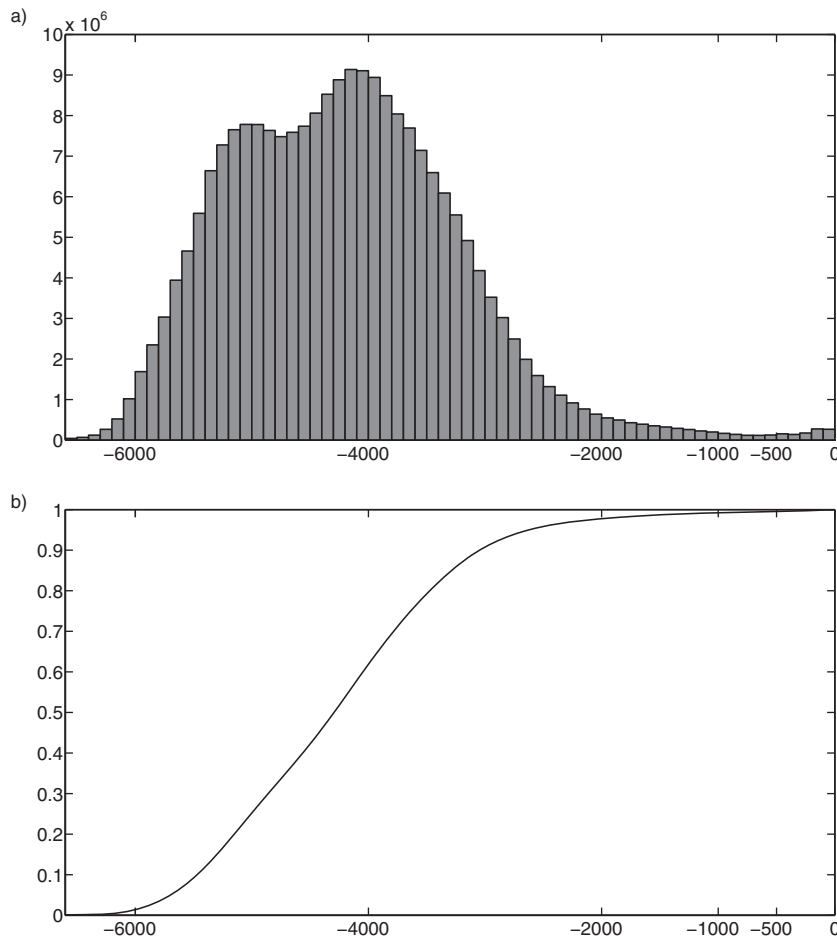


Figure 3. Abyssal hill roughness depth distribution. Histogram of the depth (in SRTM30_PLUS, in m) of grid points where abyssal hill roughness has been added. The y axis is the percentage of the ocean floor area for which synthetic abyssal hill roughness has been blended in to the SSG product. The sum of the distribution equals 100%.

SRTM30_PLUS, much more small-scale features are evident in the energy flux map (Figure 5).

3.3. Contribution of Different Topographic Scales

[30] Since the SRTM30_PLUS product sparsely resolves abyssal hills, the SRTM30_PLUS results shown in this paper do include some abyssal hill contributions. In order to isolate the abyssal hill contributions more effectively in our estimates, we compare the energy flux from the SSG bathymetry and from a version of this bathymetry where abyssal hills are gradually filtered out. More generally, using smoothed SRTM30_PLUS and SSG bathymetries with an increasing filtering window length (from 0 to 20 km) allows us to assess the contribution of different topographic scales to the energy flux. The bathymetric spectra over the MAR region after the filtering of the SSG bathymetric product are shown in Figure 6. The energy conversions calculated with the filtered bathymetries and integrated over the EPR and MAR regions are shown in Figures 7a and 7b. As expected, the energy conversion decreases when the topography is smoothed, indicating that the energy flux is increased when smaller scales of topography are resolved (Figure 5). While this is true for both the SSG and SRTM30_PLUS bathymetric products, the

decrease in the energy flux as the bathymetry is smoothed is larger for SSG (Figures 7a and 7b, continuous lines) than for SRTM30_PLUS (Figures 7a and 7b, dashed lines) due to the addition of abyssal hills in SSG. When the cutoff length of the low pass filter is longer, the abyssal hills tend to be filtered out, the two bathymetric products become similar and the energy fluxes given by the two bathymetric products converge (Figures 7a and 7b).

[31] Therefore, small-scale topography dominated by abyssal hills clearly impacts the energy conversion from barotropic to internal tides over the MAR and EPR. In these two regions, the small excursion approximation is valid (using a typical topographic length of 1 km, which roughly corresponds to the bathymetric grid size at the equator, and to the lower bound of typical abyssal hills horizontal length). However, the linear theory is strictly valid for subcritical slopes only, and abyssal hills might be dominated by supercritical slopes regionally.

3.4. Contribution of Subcritical/Supercritical Slopes

[32] Internal tide generation in the acoustic regime ($\zeta < 1$, see equation (4)) over supercritical topography is still an open question and an area of active research [Nycander, 2006; Petrelis et al., 2006; Zhang et al., 2007;

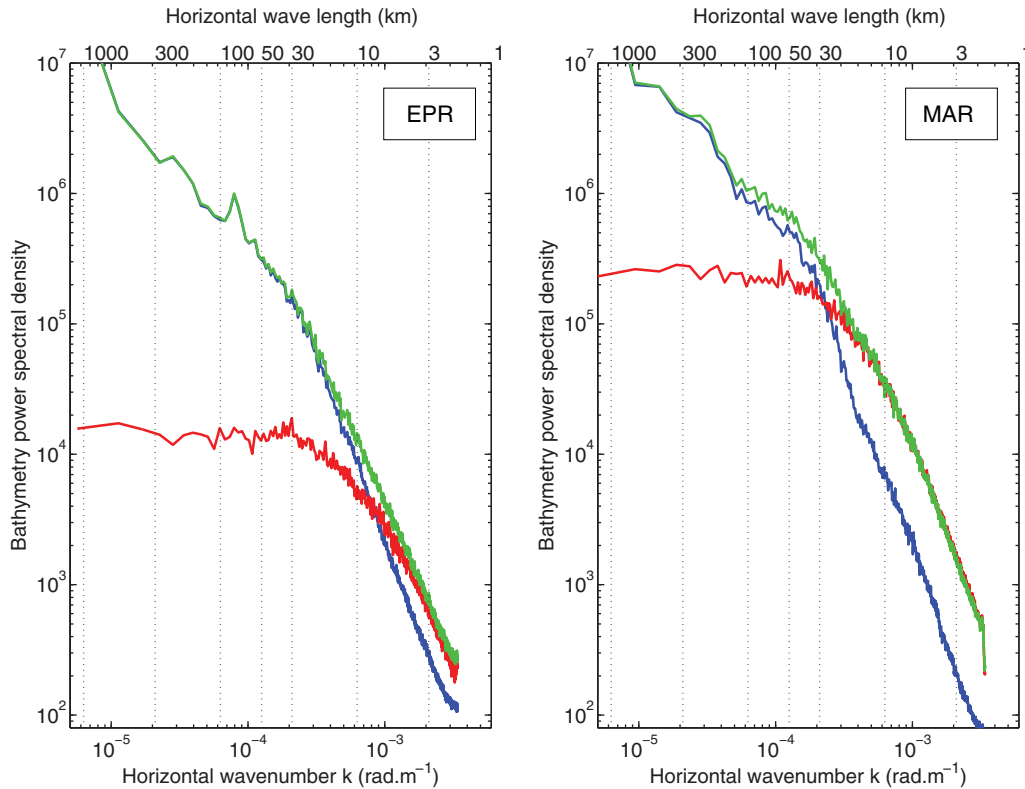


Figure 4. Bathymetric spectra in the east-west direction for the (left) EPR and (right) MAR regions for the SRTM30_PLUS (in blue), the synthetic abyssal hills (in red), and the combined SSG (in green) products. The vertical dotted lines correspond to the wavelength values labeled on the upper x axis.

Legg and Klymak, 2008; Balmforth and Peacock, 2009. Linear (i.e., subcritical) theory predicts an energy conversion proportional to Υ^2 . The scaling in the supercritical regime is unknown, but *Nycander [2006]* argued that the energy conversion saturates when the slope becomes supercritical. Some support for this is given by numerical simulations [*Khaliwala, 2003*] and analytical calculations using a periodic topography [*Balmforth and Peacock, 2009*]. Inspired by the hypothesis of *Nycander [2006]*, we will perform a crude correction for supercriticality by dividing the energy flux by Υ^2 in supercritical regions, while keeping the energy flux unchanged in subcritical regions. Critical slopes are here defined by $\Upsilon=1$. A similar correction has been used for the energy flux into atmospheric gravity waves [*Eckermann et al., 2010*], and for the energy flux into oceanic internal lee waves [*Nikurashin and Ferrari, 2010, 2011; Scott et al., 2011*]. However, it should be recognized that even if the hypotheses of saturation in the supercritical regime is correct, this method cannot be quantitatively accurate since the correction is performed locally, while the internal tide generation is a nonlocal process.

[33] In the MAR region, applying this correction for supercritical slopes makes the energy flux converge when smaller scales of the topography are resolved with both SRTM30_PLUS and SSG (Figure 7a, grey lines). The increase of the conversion achieved by resolving the smallest scales of the topography in SSG ($<O(10)$ km, compare the black lines in Figure 7a) is partially cancelled by the correction for supercritical slopes (Figure 7a, compare the black and grey continuous lines). This can be explained by

the fact that abyssal hills are responsible for a significant part of the energy conversion in MAR, but a significant fraction of abyssal hills are supercritical in this region (Figure 7c). The increase in the energy flux over the MAR region due to abyssal hills is 2.3 GW (or 64%) when the correction is applied, compared to 4.0 GW (or 89%) without the correction.

[34] In the EPR region, the correction for supercriticality also decreases the energy conversion by the resolved topography in both SRTM30_PLUS and SSG, as seen in Figure 7b (compare the continuous lines together and the dashed lines together). On the other hand, the contribution to the energy conversion from the abyssal hills is almost unaffected by this correction, as the difference between the energy fluxes from the SSG and SRTM30_PLUS bathymetries is similar with and without the correction for supercritical slopes. This is because abyssal hills over the EPR generally have subcritical slopes (Figure 7d, compare the two lines). As a result, the increase in the energy flux over the EPR region due to abyssal hills is 0.16 GW (or 30%) when the correction is applied, compared to 0.17 GW (or 23%) without the correction. Therefore, the sparse supercritical slopes in the EPR contribute to a significant fraction of the total energy flux in both SRTM30_PLUS and SSG since they are not largely found over abyssal hills.

[35] All in all, the regional calculations show that although the contribution from the abyssal hills to the total energy flux decreases when the correction for supercriticality is applied, the abyssal hills can still strongly increase the energy conversion from the M_2 barotropic tide to

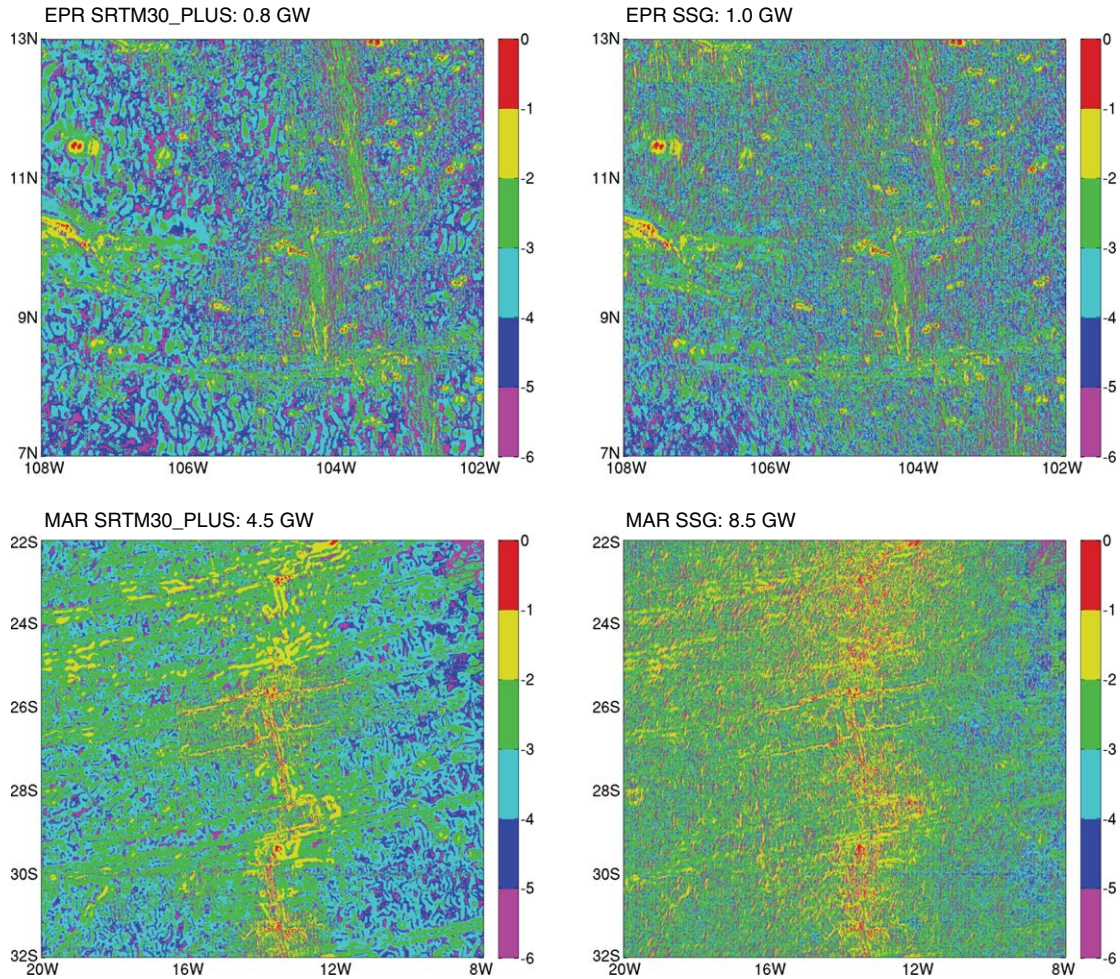


Figure 5. Regional energy fluxes. Energy flux into M_2 internal tides (in $\log_{10} \text{ W m}^{-2}$) for the (top) EPR and (bottom) MAR regions with the (left) SRTM30_PLUS and (right) SSG bathymetries. Total fluxes are given in the titles. Acoustic data cover 25% of the EPR region and 12% of the MAR region, and are mainly located over the ridges (see Figure 1).

internal tides, especially over the Mid-Atlantic Ridge. The impact is less pronounced over the EPR, but might be stronger over the Southwest Indian Ridge and the Central Indian Ridge where abyssal hill roughness is the largest (Figure 2) and tidal velocities are large.

4. Results: Global Calculation

4.1. Calculation in Real Space

[36] In this section, global calculations are performed to assess the global effect of abyssal hill roughness on internal tide generation. The global conversion of the M_2 barotropic tidal energy into internal tides based on the real-space calculation (1) with the SRTM30_PLUS bathymetry is shown in Figure 8a. The global energy flux is in good agreement with that computed by *Nycander* [2005] (see his Figure 5) using the same methodology but a coarser standard bathymetric product (SS97, *Smith and Sandwell* [1997]). Internal tides are mostly generated over continental slopes, mid-ocean ridges, and island arcs (Figure 8a). This is consistent with early estimates by *Morozov* [1995] who found that subsurface ridges, if normal to the tidal flow, can cause the

generation of large internal waves. The energy flux associated with mid-ocean ridges can exceed those generated at the coast line, which is typically parallel to the tidal flow. While the spatial distribution and levels of internal tide generation are consistent with *Nycander* [2005], it should be noted that the energy flux can reach large, unrealistic values over a few points of the ocean, especially in regions shallower than 500 m depth, or over supercritical slopes, and mostly in the Indonesian seas. In *Nycander* [2005], most of these shallow regions were excluded because of the lack of hydrographic data. The calculation of internal tide generation in shallow water is rather unreliable for three reasons: (1) the tidal velocity is larger and hence the tidal excursion is longer in shallow water region, and therefore the acoustic approximation is not valid, (2) the wave characteristics are more likely to have flatter slopes because of the stronger stratification in the thermocline, which implies that the topography is more likely to be supercritical, and (3) the tidal velocity field is less reliable in shallow water. In our estimates of the M_2 tidal energy conversion, we first use a capping of the energy flux to 1 W m^{-2} for the locations where the energy flux exceeds that value. The global

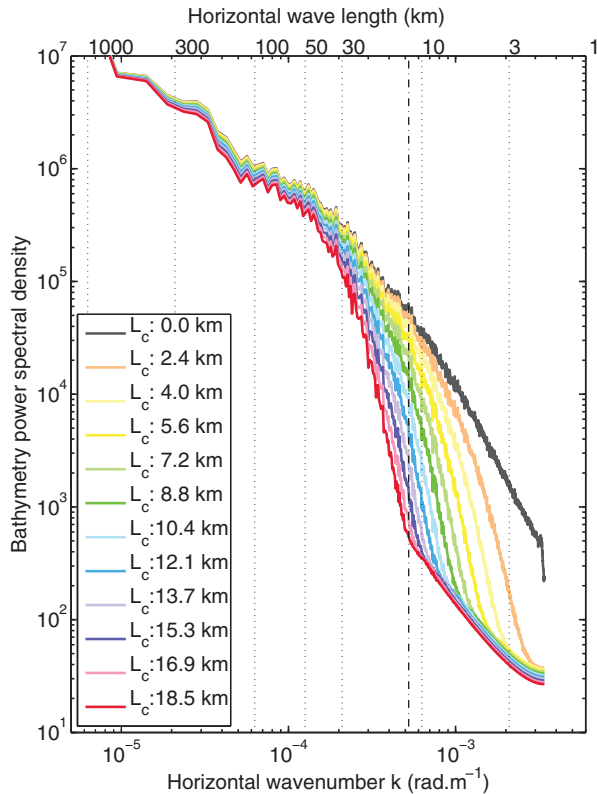


Figure 6. Spectra of the bathymetry (SSG product) in the east-west direction over the MAR region using a low-pass Hann (also known as Hanning) filter with increasing cutoff length (L_c , in km). A window length of 0 km denotes no filtering. When the filtering window length is 2.4 km, only the scales smaller than 2.4 km are removed. As the filter length increases, larger scales are removed. The vertical dashed line indicates a horizontal wavelength of 12 km (roughly the resolution of satellite-based topography), and the vertical dotted lines correspond to the wavelength values labeled on the upper x axis.

rate of the M_2 tidal energy conversion is then 1.0 TW of which 0.8 TW occurs below 500 m depth (Figure 9a). These global rates of the M_2 tidal energy conversion compare well with the estimate of 1.2 TW over the global ocean [Nycander, 2005] and of 0.6–0.8 TW in regions deeper than 500 m [e.g., Green and Nycander, 2013].

[37] The impact of abyssal hill roughness on the generation of internal tides is illustrated in Figure 8b as the difference in the global rate of the M_2 tidal energy conversion inferred from the SSG and SRTM30_PLUS bathymetric products. The global rate of the M_2 tidal energy conversion by abyssal hills is 0.08 ± 0.01 TW (Figures 8b and 9b), and is dominated by mid-ocean ridges in the Atlantic and Indian oceans, where internal tide generation due to larger topographic scales is large (Figure 8a) and abyssal hill roughness is high (Figure 2). The distribution of the global conversion rate due to abyssal hills as a function of sea floor depth (Figure 9b) reflects the distribution of abyssal hills over depth (Figure 3). Note that the results are not very sensitive to the value used for the capping of the energy flux (the choice of the capping value affects the

global conversion rate due to abyssal hills by no more than 8 GW).

[38] The energy flux into M_2 internal tides was then estimated with SRTM30_PLUS and SSG using the correction for supercritical slopes introduced in section 3.4. Indeed, compared to Nycander [2005], the higher resolution of the bathymetric products used in the present study makes it more likely for the topography to be supercritical, and for the energy flux to be overestimated. When the energy flux is weighted by the steepness parameter squared and no extra capping is used, the global rate of the M_2 tidal energy conversion using SRTM30_PLUS is 1.0 TW, of which 0.4 TW occurs below 500 m depth. Note that only a very few subcritical locations exhibit an energy flux larger than 1 W m^{-2} in the ocean deeper than 500 m, and these locations do not coincide with large abyssal hill roughness. With the correction for supercritical slope, the estimated conversion of the M_2 tidal energy by abyssal hills is 0.03 TW globally ($\sim 8\%$ of the global energy flux corrected for supercritical slope below 500m depth).

[39] Although the rate of M_2 tidal energy conversion by abyssal hills only represents a small, yet sizable, fraction of M_2 tidal energy conversion by larger topographic scales ($\sim 10\%$), the impact of abyssal hill synthetic roughness on internal tide generation can be important at regional scales, especially over mid-ocean ridges. This is especially seen in section 3 and Figures 8b and 8c.

4.2. Calculation in Spectral Space

[40] To check the robustness of our results in real space obtained from a single realization of synthetic abyssal hill topography, the energy flux from the M_2 tide into internal waves was also computed in spectral space. The global energy conversion by abyssal hills is shown in Figure 10a, and integrates to 0.08 TW. It is dominated by the Mid-Atlantic Ridge and the mid-ocean ridges in the Indian Ocean. These results are in very good agreement with those from the real space calculation (section 4.1) both in terms of the amplitude of the energy flux due to abyssal hills and of its spatial distribution (compare Figures 8b and 10a). Moreover, higher harmonics neglected in the real space calculation due to the small excursion approximation account for a minor fraction of the energy conversion in the spectral calculation, up to 5–10% regionally (Figure 10b).

[41] Note that the energy flux due to different topographies can only be added to obtain the total energy flux if the topographic features have disjoint domains in the spectral space. Indeed, the energy flux does not depend linearly on the topographic roughness (it is a quadratic function of the topographic slope). Abyssal hills added to SRTM30_PLUS and topographic features already resolved in SRTM30_PLUS roughly have distinct spatial scales or domains in the spectral space (Figure 4). Therefore, calculating the energy flux due to abyssal hills from abyssal hills alone (as done in our spectral space calculation) is not necessarily equivalent but is expected to be reasonably consistent with the subtraction of the energy fluxes inferred from the SSG and SRTM30_PLUS bathymetries (as done in our real space calculation).

5. Conclusions and Discussion

[42] Quantifying the magnitude and spatial distribution of energy conversion from barotropic tides to internal tides

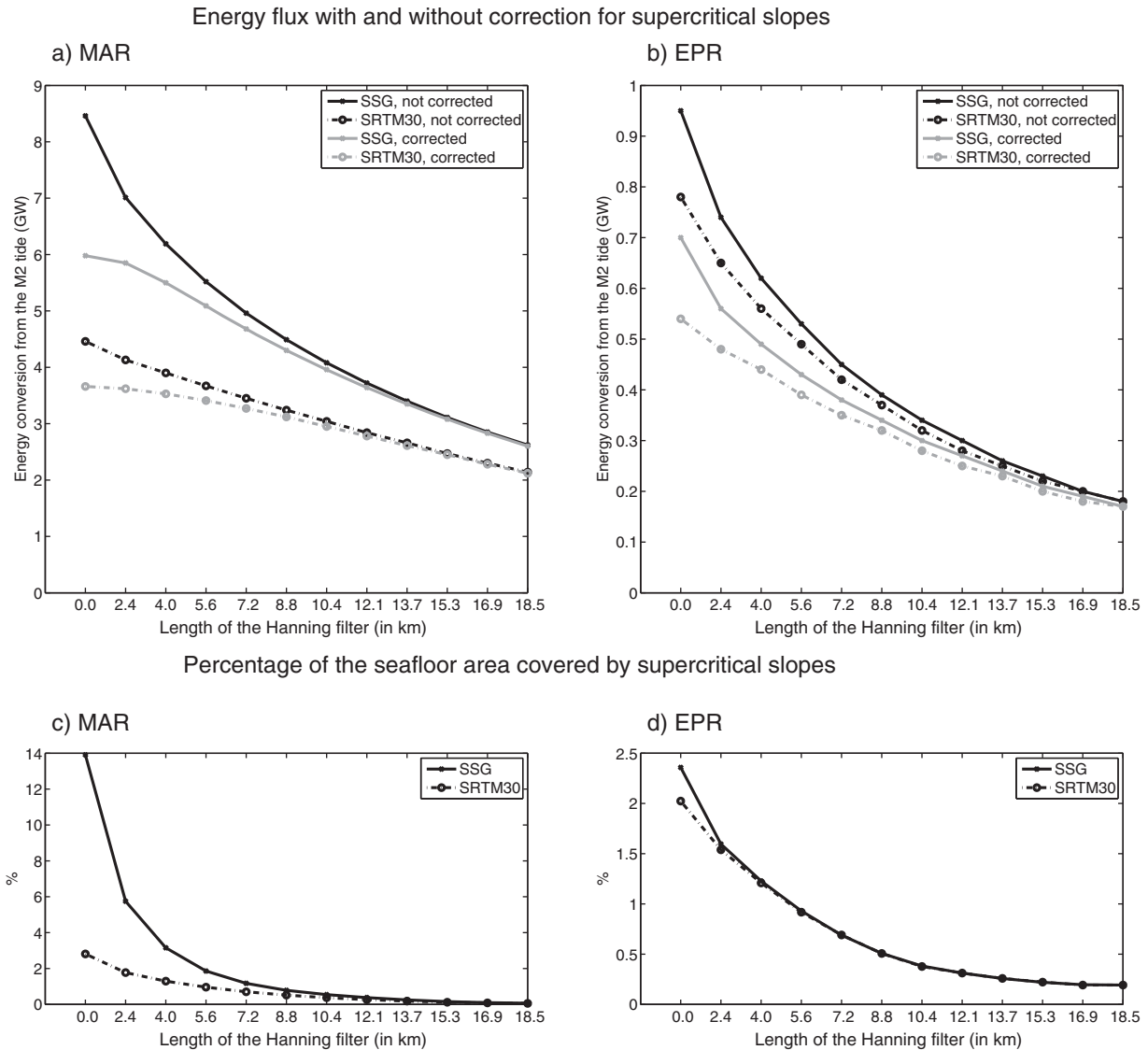


Figure 7. (top) Contribution of different topographic scales to regional energy fluxes. Energy conversion (in GW) from the M₂ tide to internal waves over (a) the MAR and (b) the EPR regions as a function of the cutoff length of the low-pass filter applied on the bathymetry. Results are shown for both the SRTM30_PLUS (dashed lines) and SSG (continuous lines) bathymetric products, without (black lines) and with (grey lines) the correction for supercritical slopes. (bottom) Percentage of the (c) MAR and (d) EPR regions seafloor area covered by supercritical slopes (in %) as a function of the cutoff length of the low-pass filter applied to the bathymetry. Results from the SRTM30_PLUS product are shown in dashed lines, while results from the SSG product are shown in continuous lines. Note the different vertical axis for the MAR and EPR regions in both the top and bottom plots.

is of importance since the dissipation of internal tide energy is a major source of mixing in the deep ocean. Internal tides are generated through the interaction of the barotropic tides with rough ocean floor topography. The relevant spatial scales of the topography for internal tide generation range from O(100) m to O(10) km. However, deep ocean bathymetry in state of the art topographic products is based primarily on satellite altimetry, which cannot resolve horizontal scales below ~ 10 km in the deep ocean. Previous studies of the energy conversion from the barotropic to internal tides at global scales were therefore limited by the resolution of the topographic

product used, and hinted that the energy conversion by unresolved topographic scales could be substantial [e.g., *Nycander, 2005*].

[43] At scales smaller than 10 km, abyssal hills are the dominant sea floor roughness fabric. Since acoustic sounding data resolving abyssal hills are not available for most of the deep ocean, synthetic maps of abyssal hill roughness have been produced based on relationships for the average statistical properties of abyssal hills as a function of sea floor spreading rate and direction. Such a map can be used as an overlay on standard coarser effective resolution topographic products.

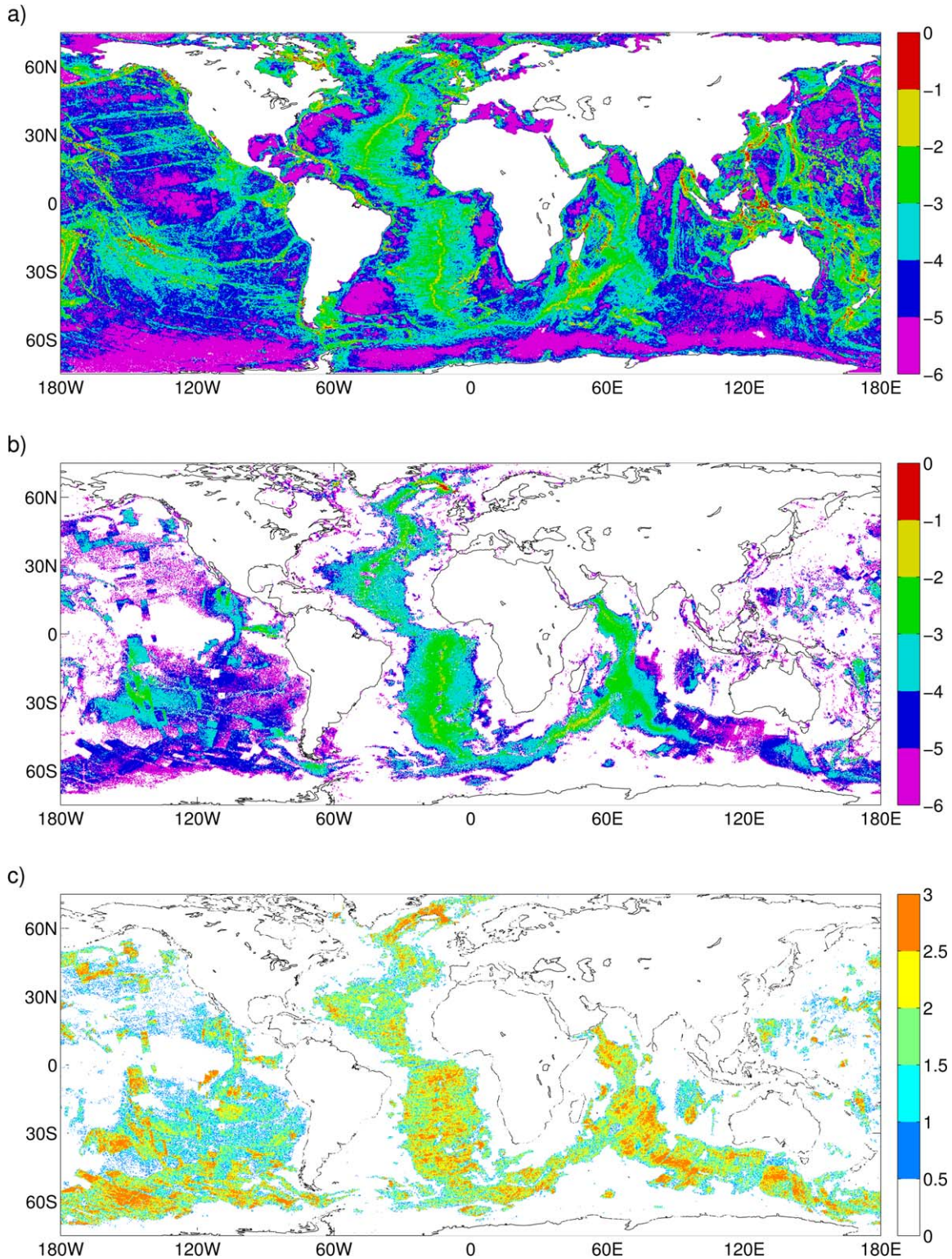


Figure 8. (a) Global energy flux from the M_2 tide into internal tides (in \log_{10} , W m^{-2}) using the SRTM30_PLUS bathymetric product, and averaged on a $1/4^\circ$ grid using an area weighted mean. (b) Abyssal hills contribution to the energy flux. Differences in the energy flux from the M_2 tide into internal tides (in \log_{10} , W m^{-2}) from the linear theory using the SSG and the SRTM30_PLUS bathymetric products (with a capping at 1 W m^{-2}), and put on a $1/4^\circ$ grid. (c) Global map of the increase in the energy flux due to abyssal hills in percentage in \log_{10} scale computed from the $1/4^\circ$ global maps of energy conversion based on SRTM30_PLUS and SSG (i.e., $\log_{10} [100 \times (E_{f\text{SSG}} - E_{f\text{SRTM30_PLUS}})/E_{f\text{SRTM30_PLUS}}]$). A doubling of the energy flux (increase of 100%) corresponds to a value of 2 in the colorbar.

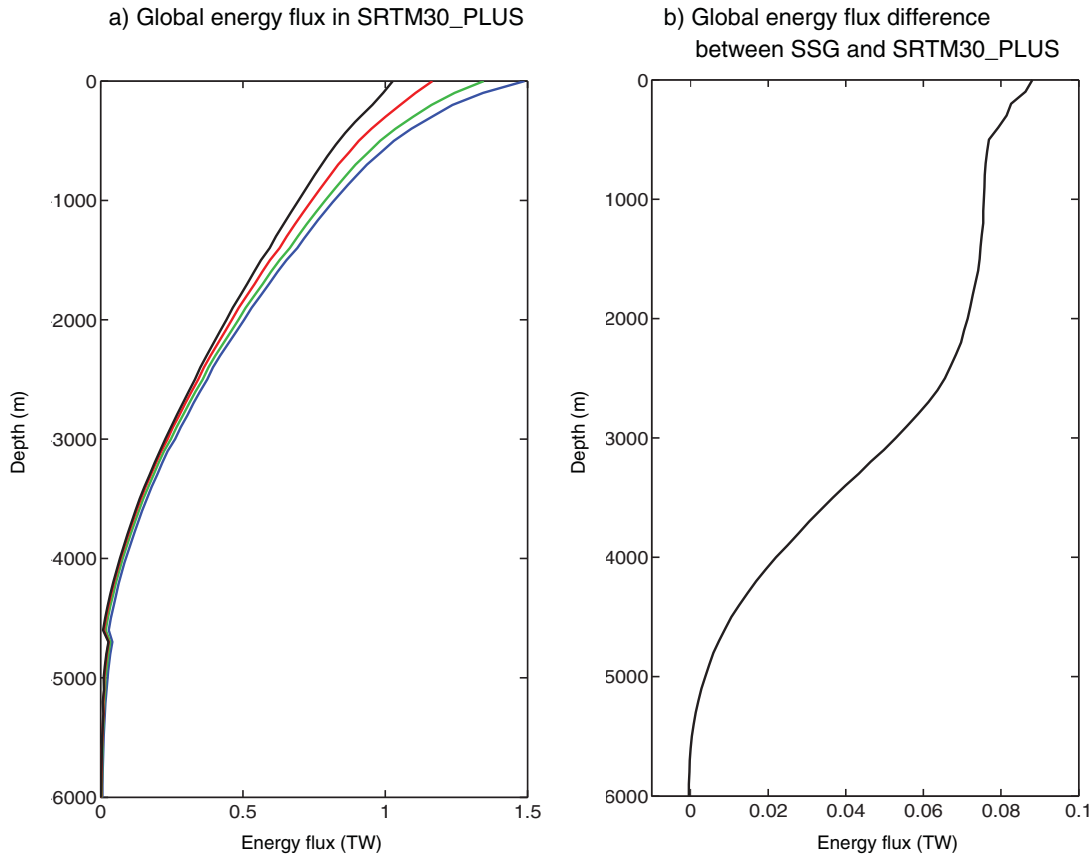


Figure 9. (a) Distribution of the global energy flux as a function of seafloor depth from the calculation using SRTM30_PLUS using a capping at 1 (black), 2 (red), 5 (green), and 10 (blue) W m^{-2} for the energy flux. (b) Distribution of the differences between the global energy fluxes calculated using SSG and SRTM30_PLUS as a function of seafloor depth using a capping at 1 W m^{-2} .

[44] In this study, we evaluate the impact of abyssal hill roughness on the energy conversion from barotropic to internal tides using linear wave theory and focusing on the M_2 tidal component. Calculations were performed both in real and spectral spaces, providing complementary information on the contribution of abyssal hills to the energy conversion. On the one hand, the calculation in real space gives an energy flux at the same resolution as the bathymetry. Calculations in real space were performed based on two global bathymetric products at a resolution of $1/120^\circ$: a state of the art product (SRTM30_PLUS) with and without the addition of a map of synthetic abyssal hill roughness. The high resolution of the bathymetric product and of the energy flux allows us to discern small-scale features in the M_2 tidal energy conversion due to the abyssal hill contribution. On the other hand, the calculation in spectral space is directly based on the spectrum of the abyssal hill bathymetry. Hence, it does not depend on a particular statistical realization of abyssal hill roughness, as the real space calculation does. Moreover, the contribution from higher harmonics can easily be computed in the spectral space.

[45] We show that the contribution of abyssal hills to the global energy flux into internal tides is 0.1 TW, with good agreement between results based on linear theory in both real and spectral spaces. Although the calculation in real

space at the global scale uses an arbitrary capping of the energy flux at 1 W m^{-2} , we believe that our results on the M_2 tidal energy conversion by abyssal hills are robust since there is only a small sensitivity to the value of the capping value (Figure 9), and the real and spectral space estimates are consistent. In addition, locations where the highest energy flux occurs are not in regions of large abyssal hill roughness. Thus, the capping affects the total level of energy conversion, but does not substantially affect the contribution from abyssal hills.

[46] Therefore, the linear theory estimate of the abyssal hills contribution to the conversion of the M_2 barotropic tides into internal tides ($\sim 0.08\text{--}0.10$ TW) represents $\sim 10\%$ of the $0.6\text{--}0.8$ TW conversion in regions deeper than 500 m by larger topographic scales [e.g., *Green and Nycander, 2013*]. The energy conversion due to abyssal hills is dominated by mid-ocean ridge regions in the Atlantic and Indian oceans, where both abyssal hill roughness and barotropic tidal velocities are large. Focusing on two regions located over the Mid-Atlantic Ridge and the East Pacific Rise, we show that regionally abyssal hills can increase the energy flux into internal tides by up to 100%. Using a low-pass filter on the bathymetry, we show that the contribution of the smallest scales of the topography (mainly abyssal hills) is significant. However, these results are only strictly valid if the topography were subcritical. Since the linear theory

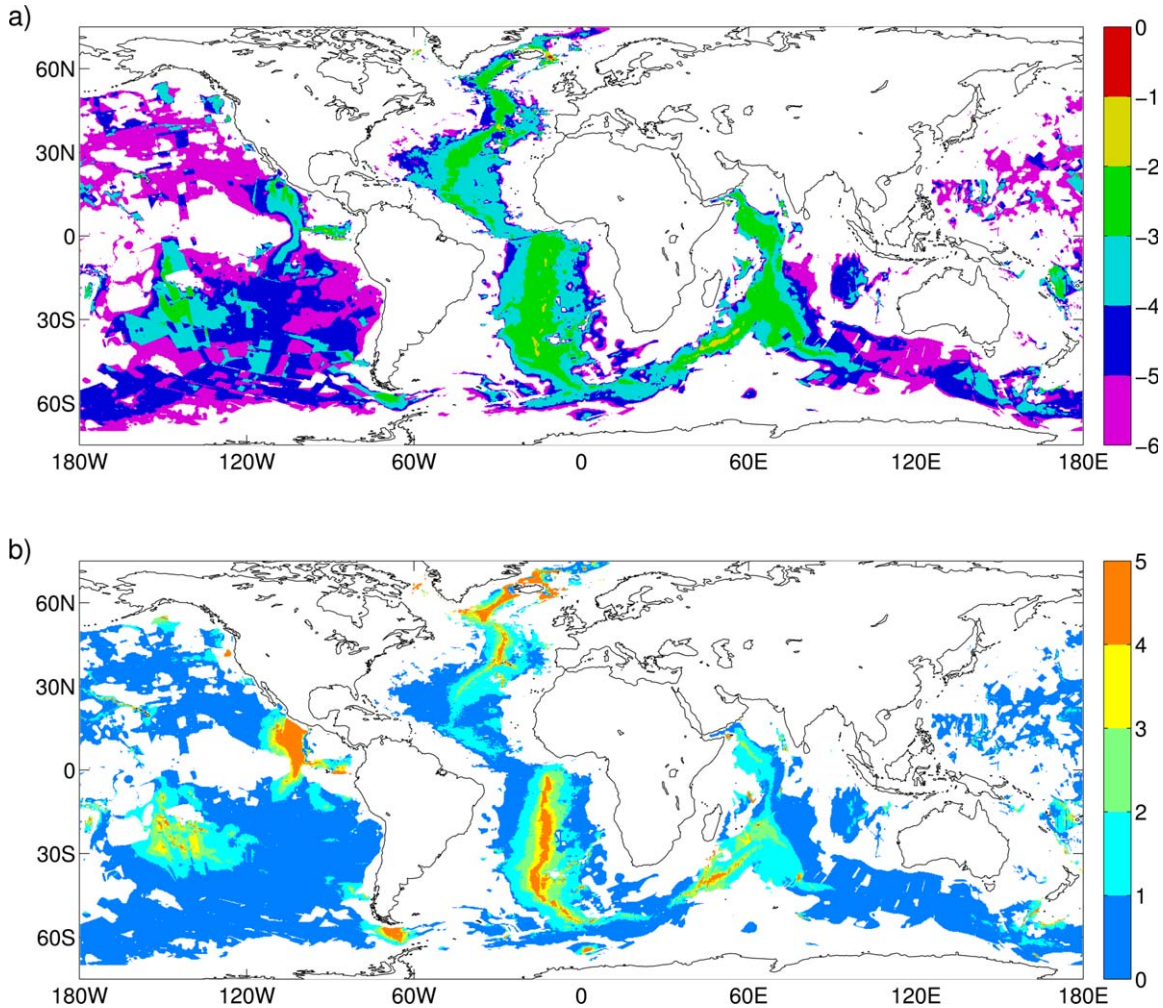


Figure 10. (top) Global energy conversion into the fundamental M_2 baroclinic tide (in \log_{10} , W m^{-2}) due to abyssal hills and calculated in spectral space. (bottom) Global energy conversion into higher M_2 harmonics ($n > 1$) normalized by the energy conversion into the fundamental M_2 frequency. Units are in %.

tends to overestimate the energy conversion over supercritical slopes, an attempt was made to correct for the contribution of supercritical slopes by normalizing the energy flux by the square of the steepness parameter to mimic energy flux saturation at supercritical slopes. With this correction, the local increase of the energy flux due to abyssal hills is in the range of 30–60% for the two regions studied here, and the abyssal hills contribution to the conversion of the M_2 barotropic tides into internal tides globally integrates to 0.03 TW.

[47] The uncertainty related to the contribution of supercritical bathymetric slopes to the energy conversion probably is the largest in this study, and more research is desirable to properly predict the energy flux into internal tides at supercritical slopes. Another source of uncertainty comes from the use of the traditional WKB approximation with the linear theory. This approximation yields an energy flux proportional to the buoyancy frequency at the ocean bottom. While this approximation holds for the high internal modes, it might not be valid for the lowest internal tide modes, where it tends to underestimate the conversion sub-

stantially [Zarroug *et al.*, 2010]. On the other hand, this will mainly affect the conversion by the resolved topography, but not that by the abyssal hills which mainly generate high modes. The synthetic realization of abyssal hill roughness used in this study provides another source of uncertainty. Notably, the map of abyssal hill roughness might be incomplete spatially (see Goff [2010] for another estimate of abyssal hill roughness with a global coverage), so that the contribution of abyssal hill roughness to internal tide generation might be underestimated in this study. Moreover, since abyssal hills are captured in a few regions by acoustic data included in SRTM30_PLUS (note areas with no synthetic abyssal hill roughness over mid-ocean ridges in Figure 2), the calculation in real space focuses on the impact of synthetic abyssal hill roughness on internal-tide generation. While this can make our estimate of the contribution from synthetic abyssal hill roughness different from the contribution from the actual abyssal hill roughness locally, we believe it will only have a small impact on the global energy conversion since acoustic data are sparse. Finally, it should be noted that the linear theory used in this

study does not allow feedback from the tidal energy conversion on the barotropic tidal velocities. In the ocean, the energy conversion into internal tides and the subsequent divergence of their momentum stresses would impact the barotropic tide. However, this is not a serious issue in our diagnostic calculation to the extent that the TPXO barotropic tidal velocity represents the observed tidal flows in the ocean. While global numerical tidal models would include these feedbacks, and therefore not suffer from a need to cap global dissipation rates as done here in our real space calculations, the limited horizontal resolution of such models is another limitation in studying the impact of abyssal hill roughness on internal tide generation. In a related paper, Timko et al. (in preparation, 2013) show that changes of the barotropic kinetic energies induced by the addition of abyssal hills remain small. Their results concur with ours in that the impact of abyssal hill roughness on internal-tide generation is small at the global scale ($\sim 5\%$ in their study), but is responsible for a large increase of the energy flux over mid-ocean ridges (up to about 25%). Therefore, although both methodologies (linear wave theory in this study, global numerical tidal model in Timko et al. (in preparation, 2013)) have known strengths and weaknesses, their qualitative agreement on the impact of abyssal hill roughness on internal tide generation gives confidence in the presented results.

[48] **Acknowledgments.** The authors would like to thank three anonymous reviewers as well as Sonya Legg for helpful comments leading to improvements in the manuscript. They also acknowledge the use of the SOSIE software for interpolation of data. The work of AM and BKA on this paper is a component of the Internal-wave driven mixing Climate Process Team funded by National Science Foundation grants OCE-0968721 and OCE-096878 and the National Oceanic and Atmospheric Administration, U.S. Department of Commerce, award NA08OAR4320752. The statements, findings, conclusions, and recommendations are those of the authors and do not necessarily reflect the views of the National Oceanic and Atmospheric Administration, or the U.S. Department of Commerce. BKA, PGT, and JAG also acknowledge support from a University of Texas Jackson School of Geosciences Development grant, Naval Research Laboratory contract N000173-06-2-C003, Office of Naval Research grants N00014-07-1-0392, N00014-09-1-1003, and N00014-11-1-0487, and National Science Foundation grant OCE-0924481.

References

Akima, H. (1970), A new method of interpolation and smooth curve fitting based on local procedures, *J. Assoc. Comput. Mach.*, *17*(4), 589–602.

Arbic, B. K., S. T. Garner, R. Hallberg, and H. L. Simmons (2004), The accuracy of surface elevations in forward global barotropic and baroclinic tide models, *Deep Sea Res. Part II*, *51*, 3069–3101.

Balmforth, N. J., and T. Peacock (2009), Tidal conversion by supercritical topography, *J. Phys. Oceanogr.*, *39*, 1965–1974.

Becker, J. J., et al. (2009), Global bathymetry and elevation data at 30 arc seconds resolution: SRTM30_PLUS, *Mar. Geod.*, *32*(4), 355–371.

Bell, T. H. (1975a), Lee waves in stratified flows with simple harmonic time dependence, *J. Fluid Mech.*, *67*, 705–722.

Bell, T. H. (1975b), Topographically generated internal waves in the open ocean, *J. Geophys. Res.*, *80*, 320–327.

Carter, G., M. Merrifield, D. Luther, J. Becker, K. Katsumata, M. Gregg, M. Levine, T. Boyd, and Y. Firing (2008), Energetics of M2 barotropic-baroclinic tidal conversion at the Hawaiian Islands, *J. Phys. Oceanogr.*, *38*, 2205–2223.

Charette, M. A., and W. H. F. Smith (2010), The volume of the Earth's ocean, *Oceanography*, *23*(2), 112–114.

Eckermann, S. D., J. Lindeman, D. Broutman, J. Ma, and Z. Boybeyi (2010), Momentum fluxes of gravity waves generated by variable Froude number flow over three-dimensional obstacles, *J. Atmos. Sci.*, *67*(7), 2260–2278.

Egbert, G. D., and S. Y. Erofeeva (2002), Efficient inverse modeling of barotropic ocean tides, *J. Atmos. Oceanic Technol.*, *19*, 183–204.

Egbert, G. D., and R. D. Ray (2000), Significant dissipation of tidal energy in the deep ocean inferred from satellite altimeter data, *Nature*, *405*, 775–778.

Egbert, G. D., and R. D. Ray (2001), Estimates of M2 tidal energy dissipation from TOPEX/Poseidon altimeter data, *J. Geophys. Res.*, *106*, 22,475–22,502.

Garrett, C., and E. Kunze (2007), Internal tide generation in the deep ocean, *Annu. Rev. Fluid Mech.*, *39*, 57–87.

Gnanadesikan, A. (1999), A simple predictive model for the structure of the oceanic pycnocline, *Science*, *283*, 2077–2079.

Goff, J. A. (1991), A global and regional stochastic analysis of near-ridge abyssal hill morphology, *J. Geophys. Res.*, *96*, 21,713–21,737.

Goff, J. A. (2010), Global prediction of abyssal hill root-mean-square heights from small-scale altimetric gravity variability, *J. Geophys. Res.*, *115*, B12104, doi:10.1029/2010JB007867.

Goff, J. A., and B. K. Arbic (2010), Global prediction of abyssal hill roughness statistics for use in ocean models from digital maps of paleo-spreading rate, paleo-ridge orientation, and sediment thickness, *Ocean Modell.*, *32*, 36–43.

Goff, J. A., and T. H. Jordan (1988), Stochastic modeling of seafloor morphology: Inversion of seabeam data for second-order statistics, *J. Geophys. Res.*, *93*(B11), 13,589–13,608.

Goff, J. A., Y. Ma, A. Shah, J. R. Cochran, and J.-C. Sempéré (1997), Stochastic analysis of seafloor morphology on the flank of the Southeast Indian Ridge: The influence of ridge morphology on the formation of abyssal hills, *J. Geophys. Res.*, *102*, 15,521–15,534.

Gouretski, V. V., and K. P. Koltermann (2004), WOCE global hydrographic climatology [CD-ROM], Ber. Bundesamt Seeschifffahrt Hydrogr. Rep. 35, 52 pp., Bundesamt Seeschifffahrt Hydrogr., Hamburg, Germany.

Green, M. J. A., and J. Nycander (2013), A comparison of tidal conversion parameterizations for tidal models, *J. Phys. Oceanogr.*, *43*, 104–119.

IOC, IHO, and BODC (2003), Centenary Edition of the GEBCO Digital Atlas [CD-ROM], Intergovernmental Oceanographic Commission and the International Hydrographic Organization as part of the General Bathymetric Chart of the Oceans, Br. Oceanogr. Data Cent., Liverpool, U. K.

Iwamae, N., and T. Hibiya (2012), Numerical study of tide-induced mixing over rough bathymetry in the abyssal ocean, *J. Oceanogr.*, *68*, 195–203.

Jayne, S. R. (2009), The impact of abyssal mixing parameterizations in an ocean general circulation model, *J. Phys. Oceanogr.*, *39*(7), 1756–1775.

Jayne, S. R., and L. C. St. Laurent (2001), Parameterizing tidal dissipation over rough topography, *Geophys. Res. Lett.*, *28*(5), 811–814.

Khatiwala, S. (2003), Generation of internal tides in an ocean of finite depth: Analytical and numerical calculations, *Deep Sea Res. Part I*, *50*, 3–21.

Legg, S., and J. M. Klymak (2008), Internal hydraulic jumps and overturning generated by tidal flow over a steep ridge, *J. Phys. Oceanogr.*, *38*, 1949–1964.

Llewellyn Smith, S. G., and W. R. Young (2002), Conversion of barotropic tide, *J. Phys. Oceanogr.*, *32*, 1554–1566.

Macdonald, K. C., P. J. Fox, R. T. Alexander, R. Pockalny, and P. Gente (1996), Volcanic growth faults and the origin of Pacific abyssal hills, *Nature*, *380*, 125–129.

Marshall, J., and K. G. Speer (2012), Closure of the meridional overturning circulation through Southern Ocean upwelling, *Nat. Geosci.*, *5*, 171–180.

Morozov, E. G. (1995), Semidiurnal internal wave global field, *Deep Sea Res. Part I*, *42*, 135–148.

Muller, C. J., and O. Bühler (2009), Saturation of the internal tides and induced mixing in the abyssal ocean, *J. Phys. Oceanogr.*, *39*, 2077–2096.

Munk, W. (1997), Once again: Tidal friction, *Prog. Oceanogr.*, *40*, 7–35.

Munk, W., and C. Wunsch (1998), Abyssal recipes II: Energetics of tidal and wind mixing, *Deep Sea Res.*, *45*, 1977–2010.

Nikurashin, M., and R. Ferrari (2010), Radiation and dissipation of internal waves generated by geostrophic flows impinging on small-scale topography: Theory, *J. Phys. Oceanogr.*, *40*, 1055–1074.

Nikurashin, M., and R. Ferrari (2011), Global energy conversion rate from geostrophic flows into internal lee waves in the deep ocean, *Geophys. Res. Lett.*, *38*, L08610, doi:10.1029/2011GL046576.

Nikurashin, M., and R. Ferrari (2013), Overturning circulation driven by breaking internal waves in the deep ocean, *Geophys. Res. Lett.*, *40*, 3133–3137, doi:10.1002/grl.50542.

- Nikurashin, M., and S. Legg (2011), A mechanism for local dissipation of internal tides generated at rough topography, *J. Phys. Oceanogr.*, *41*, 378–395.
- Nycander, J. (2005), Generation of internal waves in the deep ocean by tides, *J. Geophys. Res.*, *110*, C10028, doi:10.1029/2004JC002487.
- Nycander, J. (2006), Tidal generation of internal waves from a periodic array of steep ridges, *J. Fluid Mech.*, *567*, 415–432.
- Petrelis, F., S. Llewellyn Smith, and W. R. Young (2006), Tidal conversion at a submarine ridge, *J. Phys. Oceanogr.*, *36*(6), 1053–1071.
- Polzin, K. L. (2009), An abyssal recipe, *Ocean Modell.*, *30*(4), 298–309, doi:10.1016/j.ocemod.2009.07.006.
- Polzin, K. L., J. M. Toole, J. R. Ledwell, and R. W. Schmitt (1997), Spatial variability of turbulent mixing in the abyssal ocean, *Science*, *276*, 93–96.
- Saenko, O. A., and W. J. Merryfield (2005), On the effect of topographically enhanced mixing on the global ocean circulation, *J. Phys. Oceanogr.*, *35*, 826–834.
- Sandwell, D. T., and W. H. F. Smith (2009), Global marine gravity from retracked Geosat and ERS-1 altimetry: Ridge Segmentation versus spreading rate, *J. Geophys. Res.*, *114*, B01411, doi:10.1029/2008JB006008.
- Scott, R. B., J. A. Goff, A. C. Naveira Garabato, and A. J. Nurser (2011), Global rate and spectral characteristics of internal gravity wave generation by geostrophic flow over topography, *J. Geophys. Res.*, *116*, C09029, doi:10.1029/2011JC007005.
- Simmons, H. L., S. R. Jayne, L. C. St. Laurent, and A. J. Weaver (2004a), Tidally driven mixing in a numerical model of the ocean general circulation, *Ocean Modell.*, *6*(3–4), 245–263, doi:10.1016/S1463-5003(03)00011-8.
- Simmons, H. L., R. W. Hallberg, and B. K. Arbic (2004b), Internal wave generation in a global baroclinic tide model, *Deep Sea Res. Part II*, *51*, 3043–3068.
- Small, C., and D. Sandwell (1992), An analysis of ridge axis gravity roughness and spreading rate, *J. Geophys. Res.*, *97*(B3), 3235–3245.
- Smith, W. H. F., and D. T. Sandwell (1997), Global sea floor topography from satellite altimetry and ship depth soundings, *Science*, *277*, 1956–1962.
- St. Laurent, L. C., and C. Garrett (2002), The role of internal tides in mixing the deep ocean, *J. Phys. Oceanogr.*, *32*, 2882–2899.
- St. Laurent, L. C., and H. L. Simmons (2006), Estimates of power consumed by mixing in the ocean interior, *J. Clim.*, *19*, 4877–4890.
- St. Laurent, L. C., H. L. Simmons, and S. R. Jayne (2002), Estimating tidally driven mixing in the deep ocean, *Geophys. Res. Lett.*, *29*(23), 2106, doi:10.1029/2002GL015633.
- Talley, L. D. (2013), Closure of the global overturning circulation through the Indian, Pacific, and Southern Oceans: Schematics and transports, *Oceanography*, *26*(1), 80–97.
- Timko, P. G., B. K. Arbic, and J. A. Goff (2009), The effect of statistical abyssal hill roughness on the generation of internal waves, paper presented at 14th Layered Ocean Model Meeting, Miami, Fla.
- Toggweiler, J. R., and B. Samuels (1995), Effect of Drake Passage on the global thermohaline circulation, *Deep Sea Res. Part I*, *42*(4), 477–500.
- Zarroug, M., J. Nycander, and K. Döös (2010), Energetics of tidally generated internal waves for nonuniform stratification, *Tellus, Ser. A*, *62*, 71–79.
- Zhang, H. P., B. King, and H. L. Swinney (2007), Experimental study of internal gravity waves generated by supercritical topography, *Phys. Fluids*, *19*, 096602.